

Marco Salvato

William E. Boeing Department of
Aeronautics and Astronautics,
University of Washington,
Seattle, WA 98195
e-mail: salvato@aa.washington.edu

Kedar Kirane

Department of Mechanical Engineering,
Stony Brook University,
Stony Brook, NY 11794
e-mail: kedar.kirane@stonybrook.edu

Zdeněk P. Bažant

Department of Civil and
Environmental Engineering,
Northwestern University,
Evanston, IL 60208
e-mail: z-bazant@northwestern.edu

Gianluca Cusatis¹

Department of Civil and
Environmental Engineering,
Northwestern University,
Evanston, IL 60208
e-mail: g-cusatis@northwestern.edu

Mode I and II Interlaminar Fracture in Laminated Composites: A Size Effect Study

This work investigates the mode I and II interlaminar fracturing behavior of laminated composites and the related size effects. Fracture tests on geometrically scaled double cantilever beam (DCB) and end notch flexure (ENF) specimens were conducted. The results show a significant difference between the mode I and mode II fracturing behaviors. The strength of the DCB specimens scales according to the linear elastic fracture mechanics (LEFM), whereas ENF specimens show a different behavior. For ENF tests, small specimens exhibit a pronounced pseudoductility. In contrast, larger specimens behave in a more brittle way, with the size effect on nominal strength closer to that predicted by LEFM. This transition from quasi-ductile to brittle behavior is associated with the size of the fracture process zone (FPZ), which is not negligible compared with the specimen size. For the size range investigated in this study, the nonlinear effects of the FPZ can lead to an underestimation of the fracture energy by as much as 55%. Both the mode I and II test data can be captured very accurately by the Bažant's type II size effect law (SEL).
[DOI: 10.1115/1.4043889]

Keywords: delamination, fracture mechanics, size effect law, damage, scaling, brittleness, ductility, fiber-polymer composites, fracture testing, fracture process zone, textile reinforcement, asymptotic behavior

1 Introduction

Laminated polymer matrix composites are extensively used across the main engineering fields, from automotive, aerospace, and civil engineering to microelectronics [1–10]. This is due to their excellent in-plane mechanical properties, which make composites the material of choice for the manufacturing of large lightweight structures [2,4–6]. However, broad application of these materials is limited by their pathologically low macroscale delamination resistance, which can trigger other damage mechanisms and lead to structural collapse.

Although several approaches such as the use of three-dimensional woven and braided reinforcements [11–15], fiber stitching [16], or architected adhesives [17] have been proposed throughout the years, to mitigate this problem, the interlaminar fracture resistance remains a weakness of polymer composites. Therefore, the design of large composite structures necessitates the prediction of the critical loads for the onset of interlaminar fracturing and the related structural scaling laws. This scaling, often overlooked in the literature and practice, is the key to determine the material fracture properties governing delamination and to correlate the mechanical behavior in small-scale laboratory tests to the delamination resistance of large composite structures.

This scaling, however, cannot be captured by conventional theories such as plasticity or linear elastic fracture mechanics (LEFM). In fact, due to the emergence of several microdamage mechanisms such as the subcritical crack formation in the matrix, crack deflection, and fiber-tow bridging, the size of the fracture process zone (FPZ) in front of an interlaminar crack is often not negligible. Accordingly, the interlaminar fracturing behavior and the associated energetic size effect on structure strength can be described only if a certain length scale is linked to the finite size of the nonlinear FPZ and is used alongside the proper values of the

interlaminar fracture energy and strength. Unfortunately, estimating these material properties using standard testing procedures is quite challenging since the crack onset is often followed by snap-back instability or discontinuous crack propagation.

A possible way to overcome these issues is leveraging size effect testing [18,19]. This study presents an experimental and numerical investigation of the efficacy of the mode I and II size effect testing to characterize the interlaminar fracturing behavior of composites. It is shown that the size effect characterization enables an accurate estimation of the interlaminar fracture energy and the size of the FPZ. Furthermore, since the size effect analysis requires measuring only the peak loads, no visual inspection of the crack tip location is needed. Not only does this make size effect testing easier and more accurate than other methods, but it also allows overcoming the problems with snap-back instabilities typically afflicting mode II delamination tests.

2 Materials and Methods

2.1 Materials and Preparation. The experiments were conducted on woven composite specimens manufactured by compression molding. A DGEBA-based epoxy resin was chosen as polymer matrix, whereas the reinforcement was provided by a twill 2×2 fabric made of carbon fibers. The main in-plane mechanical properties were characterized by testing $[0 \text{ deg}]_8$ and $[45 \text{ deg}]_8$ coupons under uniaxial tension following ASTM standard procedures [20,21]. The results of this characterization are described in detail in Refs. [19,22–25] and are summarized in Table 1.

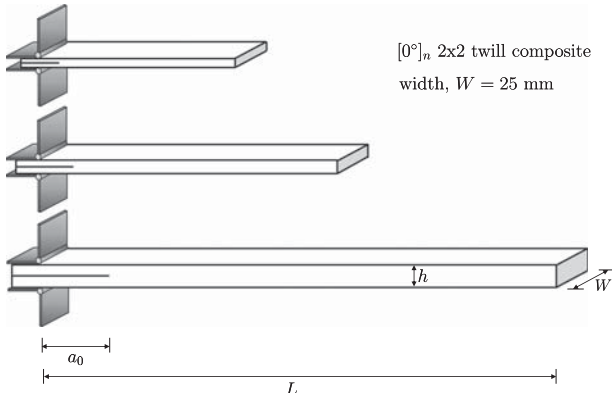
2.2 Specimen Characteristics. To investigate the interlaminar fracturing behavior of laminated composites and the related scaling, size effect tests were conducted on geometrically scaled specimens. Mode I interlaminar fracture tests were conducted on double cantilever beam (DCB) specimens, whereas the mode II interlaminar fracturing behavior was investigated using end notch flexure (ENF) specimens. For all the loading configurations, geometrically scaled specimens of three different sizes were tested. The layup was maintained as $[0 \text{ deg}]_n$ for all the tests, with n varying as a function

¹Corresponding author.

Contributed by the Applied Mechanics Division of ASME for publication in the JOURNAL OF APPLIED MECHANICS. Manuscript received April 28, 2019; final manuscript received May 24, 2019; published online June 27, 2019. Assoc. Editor: Yonggang Huang.

Table 1 Properties of carbon twill 2 × 2/epoxy composite

Description	Symbol (units)	Measured value
Fiber volume fraction	V_f (–)	0.54
Laminate thickness	t (mm)	1.9
In-plane modulus	$E = E_1 = E_2$ (GPa)	53.5
In-plane shear modulus	$G = G_{12}$ (GPa)	4.5
In-plane Poisson ratio	$\nu = \nu_{12} = \nu_{32}$ (–)	0.055
In-plane tensile strength in direction 1 and 2	$F_{11} = F_{2t}$ (MPa)	598

**Fig. 1 Geometry of the double cantilever beam (DCB) specimens under study****Table 2 Geometrical specifications of the DCB specimens under study**

Size	Thickness, h	Gauge length, L	Crack length, a_0	Width, W
Small	1.9	100	40	25
Medium	5.7	300	120	25
Large	9.5	500	200	25

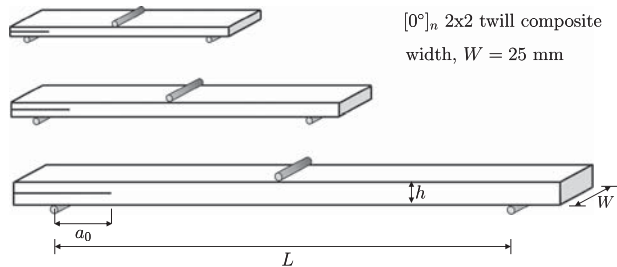
Note: Units, mm.

of the desired thickness of the specimen. For all the specimens, the initial crack was obtained by inserting a 10-μm-thick teflon film during the lamination process.

As schematically represented in Fig. 1, the smallest DCB specimen investigated in this work was made of eight layers [0 deg]₈, which resulted in total thickness $h = 1.9$ mm. Based on ASTMD5528 [26], the gauge length of the specimen was $L = 100$ mm while the width was $W = 25$ mm and the initial interlaminar crack length was $a_0 = 40$ mm. For the other specimens, all the geometrical features were geometrically scaled as 1:3:5, except for the width W , which was kept constant and equal to 25 mm (see Fig. 1). The specimen characteristics are summarized in Table 2.

Same as in Refs. [27,28], ENF specimens were used to characterize the mode II interlaminar fracturing behavior. The smallest ENF specimens featured a gauge of length $L = 200$ mm, and an initial interlaminar crack of length $a_0 = 50$ mm. For the other specimens, all the geometrical features were geometrically scaled as 2 : 3 : 5, except for the width W , which was kept constant and equal to 25 mm (see Fig. 2). The specimen characteristics are summarized in Table 3.

2.3 Testing. The DCB and ENF specimens were tested in a closed-loop servohydraulic MTS machine with a 5-kN load cell. The tests were conducted at a constant crosshead rate (stroke control, 0.5 mm/min for the smallest specimens); the rate being

**Fig. 2 Geometry of the end notch flexure (ENF) specimens under study****Table 3 Geometrical specifications of the ENF specimens under study**

Size	Thickness, h	Gauge length, L	Crack length, a_0	Width, W
Small	3.8	200	50	25
Medium	5.7	300	75	25
Large	9.5	500	125	25

Note: Units, mm.

adjusted for the different sizes to achieve roughly the same average strain rate. With such settings, the test lasted no longer than approximately 10 min for all the specimens. Stroke, force, and loading time were recorded with a sampling frequency of 10 Hz. A digital image correlation (DIC) system from correlated solutions² consisting of a 5-MP digital camera and a workstation for image postprocessing was used to measure the displacement field in the specimen with an acquisition frequency of 1 Hz.

3 Experimental Results

3.1 Mode I Interlaminar Fracture Tests. After the completion of the mode I fracture experiments, the load and displacement data were analyzed. Figure 3(a) shows, for the various investigated sizes, the typical load–displacement curves, whereas the peak loads and related structural strengths calculated as $\sigma_{Nc} = P_{max}/hW$ are summarized in Table 4. As can be noted, for all the specimen sizes investigated in this work, the structural behavior before reaching the maximum load is almost linear, with very limited damage–warming of the subsequent crack propagation. This is an indication of pronounced brittleness and of a limited effect of the nonlinear cohesive stresses in the FPZ on the structural behavior.

It is interesting that, probably due to the waviness of the tows of the twill 2 × 2 fabric, the crack propagation occurred in several unstable jumps. This phenomenon was clearly detected during the tests using DIC analysis of the displacement field surrounding the crack tip and is manifested in Fig. 3(a) by distinct load drops and recoveries after reaching the maximum load. This phenomenon, not uncommon in the delamination testing of textile composites, made the detection of the exact crack tip location very cumbersome (which is also true for, e.g., concrete). As a matter of fact, the ASTMD5528 standard [26] does not recommend the study of crack propagation by visual techniques in the presence of such behavior.

However, as it will be clear in the following, studying the fracturing behavior by size effect requires only the knowledge of the peak load. There is no need to locate the crack tip at any time. This makes the proposed methodology easier and accurate even in situations in which the visual inspection of the crack tip location is not recommended.

²<http://www.correlatedsolutions.com>

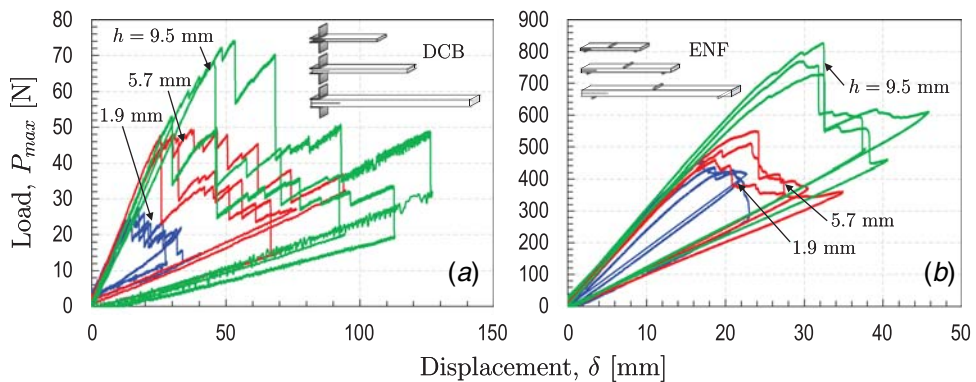


Fig. 3 Typical load–displacement curves of geometrically scaled specimens showing decreasing nonlinearity for increasing specimen dimensions: (a) DCB and (b) ENF specimens

Table 4 Results of tensile tests on double cantilever beam (DCB) specimens

Gauge length, L (mm)	Specimen thickness, h (mm)	Max. load P_{\max} (N)	Nominal strength σ_N (MPa)
100	1.9	24.18	0.490
		27.44	0.564
		30.65	0.623
300	5.7	45.16	0.302
		44.03	0.297
		47.80	0.320
500	9.5	58.18	0.226
		70.86	0.245
		53.12	0.301

Table 5 Results of tensile tests on end notch flexure (ENF) specimens

Gauge length, L (mm)	Specimen thickness, h (mm)	Max. load P_{\max} (N)	Nominal strength σ_N (MPa)
200	3.8	450	4.74
		400	4.21
		390	4.11
300	5.7	512	3.59
		551	3.86
		460	3.24
500	9.5	828	3.49
		730	3.08
		769	3.28

3.2 Mode II Interlaminar Fracture Tests. The load–displacement curves obtained from the ENF tests are represented in Fig. 3(b) for all the specimen sizes while Table 5 summarizes the peak loads and structural strengths, $\sigma_{Nc} = P_{\max}/hW$, reported in the tests. It is interesting to note that, in contrast to the DCB specimens, the load–displacement curves of the ENF specimens exhibit a more pronounced nonlinear behavior before the peak load. This phenomenon, which is more significant for small specimen sizes, is related to the formation of a nonlinear FPZ whose size is not negligible compared with the structure size. For sufficiently small specimens, the nonlinear damage in the FPZ in the form of subcritical, matrix microcracking [29], crack deflection, and fiber pullout can affect the structural behavior significantly. A typical process of formation of an FPZ under mode II loading conditions in thermoset polymers is schematically represented in Fig. 4(a).

It is worth noting from Fig. 3(b) that the mode II interlaminar crack propagating unstably right after the peak load was observed for all the investigated sizes. This unstable crack propagation is associated with a snap-back instability, as indicated by the sudden drop of the load after the peak. It should be highlighted here that the snap-back instability makes the calibration of cohesive laws for mode II delamination particularly challenging. In fact, since the load frame cannot follow the equilibrium load path (curve ABC in Fig. 4(b)), the measured load–displacement curve exhibits a sudden dynamic drop schematized by the vertical segment AC in Fig. 4(b). Accordingly, the shaded area ABC in Fig. 4(b) represents the kinetic energy imparted to the system by the load frame. Calibrating the cohesive law such that the experimental curve be matched exactly cannot lead to an accurate characterization of the cohesive behavior since it only allows estimating an upper bound for the initial fracture energy. On the other hand, leveraging only the data after the snap-back instability to infer the cohesive behavior can lead only to the calibration of the parameters describing the last

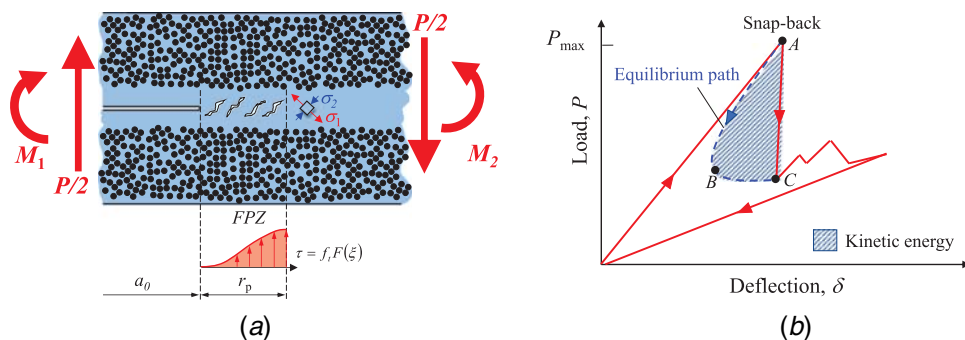


Fig. 4 (a) Schematic representation of the damage mechanisms in the FPZ of a mode II interlaminar crack leading to the emergence of nonlinear cohesive shear stresses and (b) schematic illustration of the snap-back instability affecting the ENF tests

part of the cohesive law, which controls the formation of the fully developed FPZ.

The size effect tests presented in this work allow overcoming the foregoing issues since they require only the characterization of the peak load for geometrically scaled specimens of different sizes. Thanks to this procedure, the initial mode II fracture energy can be easily estimated using the equations presented in the next sections. Further, this information can be used to estimate the initial part of the cohesive curve precisely, using the approach outlined by Cusatis and Schauffert [30].

4 Analysis and Discussion

In polymer composites, the size of the nonlinear FPZ emerging close to the tip of an interlaminar crack is generally significant compared with the structure size. In fact, discontinuous cracking, micro-crack deflection, microcrack pinning, or fiber/tow bridging of the crack [29,31] lead to highly nonlinear cohesive stresses. This scenario cannot be captured by LEFM since it assumes the effects of the nonlinear zone to be negligible. To capture the nonlinear stresses close to the crack tip, a characteristic length scale associated with the size of the FPZ must be introduced [18,19,29–37]. This is detailed in the following sections.

4.1 Size Effect Law for Mode I and II Interlaminar Fracturing in Composites. In quasi-brittle composites, the effects of the nonlinear FPZ on the interlaminar fracturing behavior can be analyzed leveraging an equivalent linear elastic fracture mechanics approach. An effective crack length $a = a_0 + c_f$ with a_0 = initial crack length and c_f = effective FPZ length is introduced. According to LEFM, the energy release rate can be written as follows:

$$G^{(i)}(\alpha) = \frac{\sigma_N^2 h}{E^*} g_{(i)}(\alpha) \quad (1)$$

where $\alpha = a/h$ is the normalized effective crack length, $\sigma_N = P/Wh$ is the nominal stress, E^* is the equivalent elastic modulus, and $g_{(i)}(\alpha)$ is the dimensionless energy release rate for mode i . The failure condition, assuming that $g'_{(i)}(\alpha) > 0$ (i.e., the structure has positive geometry [18]), can now be written as

$$G^{(i)}\left(a_0 + c_f^{(i)}/h\right) = \frac{\sigma_N^2 h}{E^*} g_{(i)}\left(a_0 + c_f^{(i)}/h\right) = G_f^{(i)} \quad (2)$$

where $G_f^{(i)}$ with $i = I, II$ is the mode- i fracture energy of the material and $c_f^{(i)}$ is the effective FPZ length, assumed to be a material property.

By expanding $g_{(i)}(\alpha)$ in Taylor series at α_0 and retaining only the terms up to the first order, one obtains

$$G_f^{(i)} = \frac{\sigma_N^2 h}{E^*} \left[g_{(i)}(\alpha_0) + \frac{c_f^{(i)}}{h} g'_{(i)}(\alpha_0) \right] \quad (3)$$

which can be rearranged as follows [18]:

$$\sigma_{Nc} = \sqrt{\frac{E^* G_f^{(i)}}{h g_{(i)}(\alpha_0) + c_f^{(i)} g'_{(i)}(\alpha_0)}} \quad (4)$$

Here, $g'_{(i)}(\alpha_0) = dg_{(i)}(\alpha_0)/d\alpha$.

The foregoing equation links the nominal strength σ_{Nc} of radially scaled structures to a characteristic length h . An alternative way to write this expression is as follows:

$$\sigma_{Nc} = \frac{\sigma_0^{(i)}}{\sqrt{1 + h/h_0^{(i)}}} \quad (5)$$

where $\sigma_0^{(i)} = \sqrt{E^* G_f^{(i)} / c_f^{(i)} g'_{(i)}(\alpha_0)}$. Further, $h_0^{(i)} = c_f^{(i)} g'_{(i)}(\alpha_0) / g_{(i)}(\alpha_0)$ is a constant, which depends on the FPZ size as well as the specimen geometry. In contrast to LEFM, Eq. (5) features a characteristic length scale $h_0^{(i)}$, which is quintessential to capture the transition

from quasi-ductile to brittle behavior with increasing structure size, reported especially in the mode II fracture tests.

4.1.1 Size Effect Analysis of the Experimental Data. Following Bažant and Kazemi [33] and Bažant and Planas [18], the following transformation is used to identify the values of $G_f^{(i)}$ and $c_f^{(i)}$ from the experiments:

$$X = h, \quad Y = \sigma_{Nc}^{-2} \quad (6)$$

$$\sigma_0^{(i)} = [C^{(i)}]^{-1/2}, \quad h_0^{(i)} = \frac{C^{(i)}}{A^{(i)}} = \frac{1}{A^{(i)} [\sigma_0^{(i)}]^2} \quad (7)$$

Accordingly, Eq. (5) takes now the following form:

$$Y = A^{(i)} X + C^{(i)} \quad (8)$$

which can be used to perform a linear regression analysis of the experimental values of the nominal strength. It is worth mentioning, however, that Eq. (8) is based on the assumption that all the specimens are scaled exactly. This means that $g_{(i)}(\alpha_0)$ and $g'_{(i)}(\alpha_0)$ take the same values for all the specimen sizes (generalization to dissimilar specimens has also been demonstrated but requires calculating different g values for different specimens or sizes).

Once the values of the parameters $A^{(i)}$ and $C^{(i)}$ are calculated, the mode- i fracture energy of the material $G_f^{(i)}$ and the effective FPZ size $c_f^{(i)}$ can be obtained as follows:

$$G_f^{(i)} = \frac{g_{(i)}(\alpha_0)}{E^* A^{(i)}}, \quad c_f^{(i)} = \frac{C^{(i)} g_{(i)}(\alpha_0)}{A^{(i)} g'_{(i)}(\alpha_0)} \quad (9)$$

However, the foregoing equations urge the computation of the functions $g_{(i)}(\alpha)$ and $g'_{(i)}(\alpha) = dg_{(i)}(\alpha)/d\alpha$. This is the subject of the next section.

4.2 Calculation of $g_{(i)}(\alpha)$ and $g'_{(i)}(\alpha)$. Function $g_{(i)}(\alpha)$ can be obtained through finite element (FE) analyses. In this work, the simulations were performed in ABAQUS IMPLICIT 6.13 [38] using eight-node biquadratic plain strain quadrilateral elements (CPS8), combined with the quarter-element technique [39] at the crack tip to provide accurate results. About 330,000 elements were used for the whole model, the smallest element size at the tip being about $a_0 \cdot 10^{-5}$. An orthotropic, linear elastic, constitutive law was used for the simulations, with $E_1 = 53,500$ MPa, $E_2 = 10,000$ MPa, and $v_{12} = 0.3$. As shown in Figs. 5(a) and 5(b), directions 1 and 2 were longitudinal and orthogonal to the axis of the specimen, respectively. The energy release rate for both the DCB and ENF specimens was estimated via the calculation of the J-integral [40].

A representation of the meshes used in this work and of a typical contour plot of the maximum principal strain close to the crack tip is provided in Figs. 5(a) and 5(b). It may be mentioned that, for the simulation of the ENF specimens, the general contact formulation with penalty stiffness available in ABAQUS/IMPLICIT [38] was used to capture the frictional phenomena occurring between the crack surfaces. A friction coefficient $\mu = 0.3$ was used, although a comprehensive parametric study revealed that the energy dissipated by friction does not have a significant effect on the calculation of the energy release rate. In fact, the normal component of the forces acting on the crack surfaces in the incipient failure condition was found to be negligible.

Finally, it should also be noted that the FE simulations allowed accounting explicitly for the rotation of the arms of the DBC specimens at the crack tip without the need of correction factors or approximations [41,42].

After calculating the J-Integral from FEA, the following expression based on LEFM was used to calculate the value of $g_{(i)}(\alpha)$:

$$g_{(i)}(\alpha) = \frac{G^{(i)}(\alpha) E^*}{h \sigma_N^2} \quad (10)$$

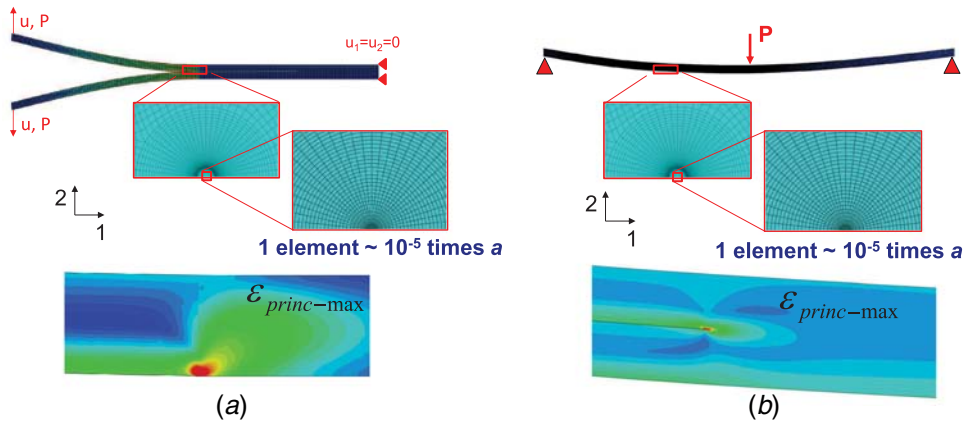


Fig. 5 Schematic representation of the linear finite element model for the calculation of $g(\alpha)$ and $g'(\alpha)$ and typical maximum principal strain fields: (a) DBC and (b) ENF specimens

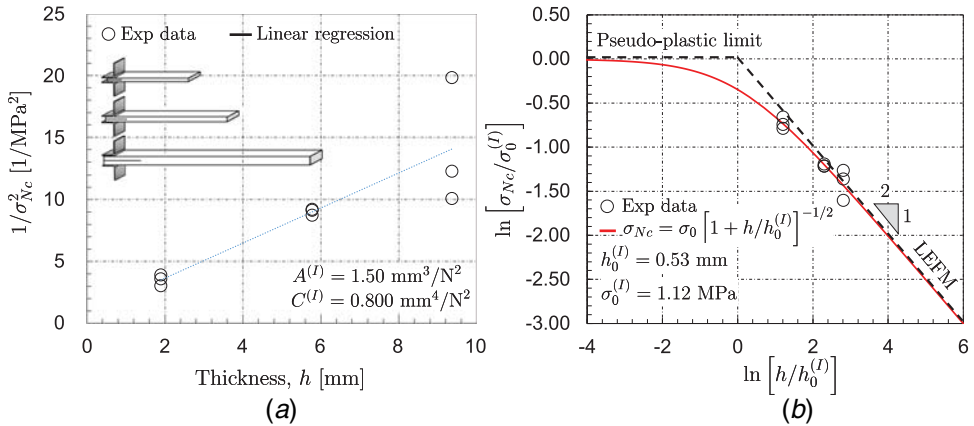


Fig. 6 Size effect study: (a) linear regression analysis to characterize the size effect parameters and (b) size effect plot in mode I interlaminar fracture

In the foregoing expression $\sigma_N = P/Wh$, P is the applied load, W is the width, and $\alpha = a/h$ is the dimensionless normalized relative crack length. For all the calculations of the dimensionless energy release functions, the condition $E^* = E_1$ was used.

To calculate $g'_{(I)}(\alpha)$, various normalized crack lengths close to the selected value of α were simulated to calculate the tangent slope of $g_{(I)}(\alpha)$ through linear interpolation [19].

Following the foregoing procedure, the values of the dimensionless energy release rate functions for the mode I interlaminar crack were found to be $g_{(I)}(\alpha_0) = 45019.9$ and $g'_{(I)}(\alpha_0) = 4125.8$ with $\alpha_0 = a_0/h = 21.05$. For the ENF specimens, on the other hand, $g_{(II)}(\alpha_0) = 807.0$ and $g'_{(II)}(\alpha_0) = 120.4$ with $\alpha_0 = a_0/h = 13.16$.

4.3 Analysis of the Mode I Interlaminar Fracture Tests by the Size Effect Law. The mode I interlaminar fracture tests were analyzed by means of the type II size effect law (SEL) outlined in the foregoing sections. Figure 6(a) shows the linear regression analysis based on the transformation reported in Eq. (6). This led to the identification of the following parameters: $A^{(I)} = 1.50 \text{ mm}^3/\text{N}^2$ and $C^{(I)} = 0.800 \text{ mm}^4/\text{N}^2$. As can be noted, the SEL is in very good agreement with the experimental data, notwithstanding the scatter of the data on the large size specimens.

The results of the linear regression analysis can be used along with Eqs. (7a) and (7b) to estimate the values of the quasi-plastic limit under mode I loading $\sigma_0^{(I)}$ and the transitional thickness $h_0^{(I)}$ marking transition from quasi-ductile to brittle structural behavior. Based on the tests conducted in this work, it was found that

$\sigma_0^{(I)} = 1.12 \text{ MPa}$ and $h_0^{(I)} = 0.53 \text{ mm}$. Using Eqs. (9a) and (9b), the estimated mode I fracture energy and related equivalent FPZ length are $G_f^{(I)} = 0.56 \text{ N/mm}$ and $c_f^{(I)} = 5.82 \text{ mm}$, respectively.

Figure 6 shows the best fit of the experimental nominal strength by the size effect law, Eq. (4) or (5). As can be noted, the normalized strength $\sigma_{NC}/\sigma_0^{(I)}$ is plotted as a function of the normalized characteristic thickness $h/h_0^{(I)}$ in double logarithmic scale. The SEL exhibits two important asymptotes. The horizontal asymptote represents the structural strength predicted by plastic limit analysis, for which the failure of geometrically similar structures should always occur when $\sigma_{NC} = \sigma_0^{(I)}$ and thus implies no scaling. In contrast, the asymptote of inclination $-1/2$ (in log-log scale) represents the structural strength predicted by the LEFM according to which the strength scales with $h^{-1/2}$. The intersection of the two asymptotes corresponds to the transitional thickness $h_0^{(I)}$, which marks the transition from quasi-plastic to brittle behavior for increasing specimen sizes.

It is important to note that the structural strength of all the DCB specimens investigated follows the LEFM asymptote relatively closely, which means that the nonlinear cohesive stresses in the FPZ do not affect significantly the structural behavior for the specimens of the sizes investigated in this work or larger. This is also confirmed by the relatively good agreement between the mode I fracture energy value estimated by the SEL and its value estimated by the LEFM, which is $G_{f,LEFM}^{(I)} = \sigma_{NC}^2 h/E^* g_{(I)}(\alpha_0)$. The LEFM predicts fracture energy values $G_{f,LEFM}^{(I)} = 0.46, 0.54$, and 0.55 N/mm for the small, medium, and large sizes, respectively. Although the values estimated by the LEFM are slightly size dependent, the

difference compared with SEL is always within the scatter of the experimental data, especially for the medium and large size specimens.

The foregoing results confirm that, as suggested by the ASTMD5528 [26], LEFM can be used to accurately predict the mode I delamination onset of the twill 2×2 specimens investigated in this work, as well as the related scaling.

The nonlinear effects of the FPZ would start to be significant only for ultrathin composite structures [43,44] whose thickness is typically lower than the transitional one: $h < h_0^{(I)} = 0.53$ mm.

4.4 Analysis of the Mode II Interlaminar Fracture Tests by the Size Effect Law. The mode II SEL formulated in the foregoing sections was used to analyze the tests on the ENF specimens, following a procedure similar to that described for the analysis of the DCB specimens. Figure 7(a) shows the linear regression analysis leveraging the transformation reported in Eq. (6), with $A^{(II)} = 6.70 \cdot 10^{-3} \text{ mm}^3/\text{N}^2$ and $C^{(II)} = 3.35 \cdot 10^{-2} \text{ mm}^4/\text{N}^2$. As can be noted, also in this case, the SEL is in excellent agreement with the experimental data, and the fitting enables estimating the quasi-plastic limit under mode II loading $\sigma_0^{(II)}$ and the transitional thickness $h_0^{(II)}$ by means of Eqs. (7a) and (7b). Based on the tests conducted in this work, it is found that $\sigma_0^{(II)} = 5.46$ MPa and $h_0^{(II)} = 5.00$ mm. On the other hand, the mode II fracture energy and related equivalent FPZ length are $G_f^{(II)} = 2.25$ N/mm and $c_f^{(II)} = 33.51$ mm, respectively.

Figure 7(b) shows the normalized strength $\sigma_{NC}/\sigma_0^{(II)}$ against the normalized characteristic thickness $h/h_0^{(II)}$ in double logarithmic scale and the best fit by the size effect law, Eq. (4) or (5). It is interesting to note that, in contrast to the results on the DCB specimens, the structural strength values of the ENF specimens lie right at the transition between the pseudoplastic and the LEFM asymptotes.

This observation confirms that the structural behavior of the ENF specimens is much more influenced by the strain redistribution caused by the damage in the FPZ and that the resulting structural behavior is much more quasi-ductile. Due to the presence of a characteristic length scale $c_f^{(II)}$ associated with the size of the FPZ, the SEL can capture the experimental data with excellent accuracy, as shown in Fig. 7(b). The same cannot be said of the LEFM nor the plasticity theory, which both lack of a characteristic length scale and thus cannot capture the transition from quasi-ductile to brittle behavior, as demonstrated in the ENF tests.

It is worth noting that the use of LEFM to estimate the mode II fracture energy would lead to size-dependent values, $G_{f,LEFM}^{(II)}$ being equal to 1.02, 1.28, and 1.36 N/mm for the small, medium, and large size specimens, respectively. This is a serious issue since it contradicts the fundamental assumption of LEFM that $G_f^{(II)}$ is a material property. More importantly, the values of the

fracture energy predicted by the LEFM are 54.9%, 43.0%, and 39.8% lower than the value provided by the SEL depending on the specimen size.

4.5 Finite Element Analysis of the Experiments Via a Cohesive Zone Model. To validate the mode I and II fracture energies estimated by SEL, a finite element analysis was conducted. The same mesh and boundary conditions as described in Sec. 4.2 were used, whereas the cohesive stresses on the crack surfaces were captured by the standard cohesive interaction algorithm available in ABAQUS/IMPLICIT [38]. Due to the fine mesh, the cohesive stresses in the FPZ were always described by at least 50 elements for any size and for both the DCB and ENF specimens. In the absence of additional information on the exact shape of the cohesive curve, the traction-separation law was supposed to be linear for both mode I and II loading.

The fracture energies used in the cohesive law were taken directly from SEL whereas the cohesive strength was calibrated to provide the best match of the experimental data, leading to a strength of 10 MPa, for both the mode I and the mode II cohesive laws. As can be noted from Fig. 8, which shows a comparison between the experimental and predicted load displacement curves for the DCB specimens, the agreement with the test in terms of peak load is excellent. Further, the cohesive zone model (CZM) was able to capture fairly well also the load–displacement evolution during crack propagation for all the specimen sizes.

It should be mentioned that the jumps in crack propagation could not be captured by the model since the top and bottom layers of the

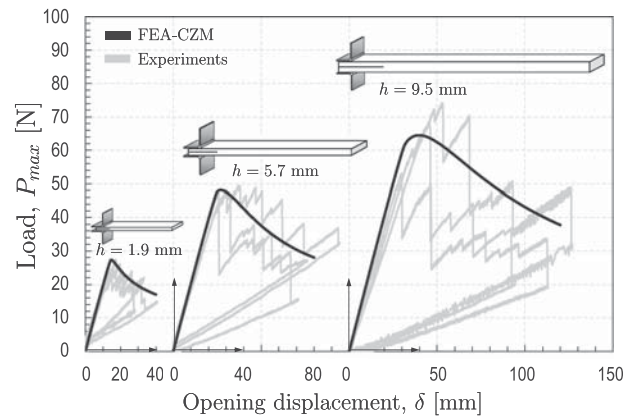


Fig. 8 Simulations by means of a cohesive zone model (CZM) with a linear traction-separation law. The mode I fracture energy used as input is estimated by means of size effect law (SEL)

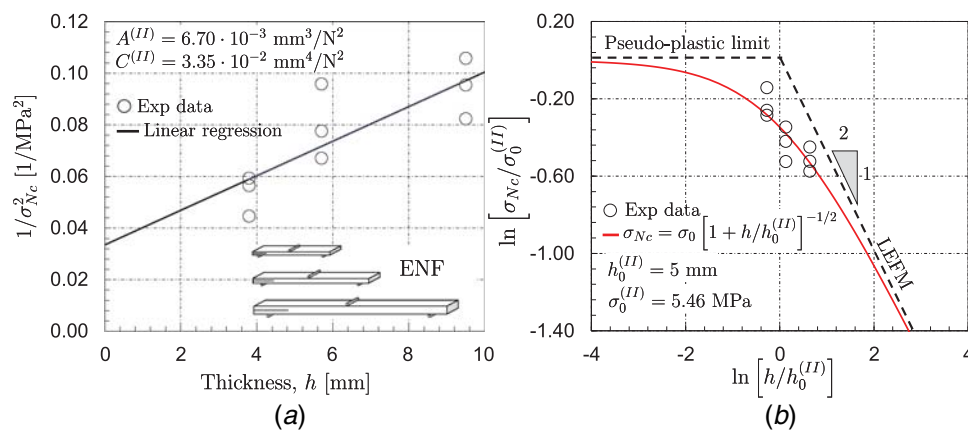


Fig. 7 Size effect study: (a) linear regression analysis to characterize the size effect parameters and (b) size effect plot in mode II interlaminar fracture

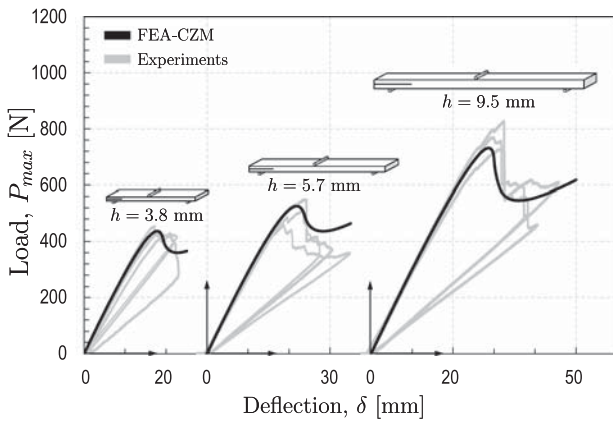


Fig. 9 Simulations by means of a cohesive zone model (CZM) with a linear traction-separation law. The mode II fracture energy used as input is estimated by means of size effect law (SEL)

FE mesh treated the composite as a homogenized continuum. Accordingly, phenomena such as crack deflection due to the waviness of the fabric were not considered explicitly. Also, it should be mentioned that an even better prediction of the crack propagation stage could have been achieved by using a different traction-separation law. In fact, recent results by Qiao and Salvati [36] have shown that the cohesive behavior of thermoset polymers is best described by a bilinear traction-separation law featuring a steep decrease of the cohesive stresses in the first part of the curve followed by a milder reduction in the second (tail) branch of the cohesive law [37] (this is similar to the cohesive softening law shape experimentally identified for concrete [45]).

Similar conclusions can be drawn for the ENF simulations. As shown in Fig. 9, the agreement between the finite element simulation and the test data in terms of peak loads is excellent. Moreover, also the post-peak behavior is captured very well with the predicted load-displacement curves becoming steeper and steeper with increasing specimen size. As can be noted from the experimental data, snap-back instability was occurring in the medium and large size specimens while the model predicted a steep but stable decrease of the load. Again, this may be due to the use of a linear, mode II cohesive law. The use of a bilinear law with a steeper decrease of the shear stresses in the initial phase would lead to the prediction of a snap-back instability as well.

The foregoing results are particularly important for the calibration of advanced computational models for composites. They confirm that the energy estimated by SEL, and not the one calculated by LEFM, should be used as input in advanced computational models for composites.

5 Conclusions

The present investigation of the mode I and II interlaminar fracturing behavior of laminated composites and the related size effect leads to the following conclusions:

- (1) The fracture tests on radially scaled DCB and ENF specimens confirm a remarkable size effect for both mode I and II interlaminar fracturing. For the size range investigated in this work, the fracture scaling of the mode I interlaminar specimens is captured accurately by the LEFM. In contrast, mode II fracture exhibits a different scaling. The double logarithmic plots of the nominal stress as a function of the characteristic size of the specimens show that the fracturing behavior evolves from quasi-ductile to brittle with increasing sizes. This is associated with a more pronounced quasi-ductility.

- (2) Numerical simulations confirm that the more pronounced quasi-brittleness of the ENF specimens is not associated with the frictional stresses acting on the crack surfaces.
- (3) The particular scaling of the ENF experiments is related to the size of the FPZ. In mode I loading, the FPZ is generally very small compared with the specimen sizes tested in this work. Since LEFM is based on the assumption of negligible nonlinear effects in the FPZ, it can capture the experiments fairly well. However, the damage mechanisms such as matrix microcracking (Fig. 4(a)), crack deflection, and plastic yielding occurring under mode II loading lead to a significantly larger FPZ. For sufficiently small ENF specimens, the size of the highly nonlinear FPZ is not negligible compared with the specimen characteristic size, and thus highly affects the fracturing behavior. This results into a significant deviation from the LEFM.
- (4) Understanding the scaling of the interlaminar fracturing behavior and developing rigorous fracture mechanics models is key for the structural design of laminated composite structures. At the same time, the analysis of the scaling of the fracturing behavior is fundamental to estimate the mode I and II fracture energies. The analysis of the present results shows that the LEFM provides a relatively accurate description of the fracturing behavior and its scaling under mode I loading. In contrast, using LEFM to calculate the mode II fracture energy from the experiments leads to a size-dependent $G_f^{(II)}$. This is because LEFM lacks a characteristic fracture length and thus cannot capture the effects of the FPZ size. As a consequence, the fracture energy obtained according to LEFM was 1.01 N/mm, 1.28 N/mm, and 1.36 N/mm for the small, medium, and large sizes, respectively.
- (5) To overcome the limitations of LEFM, an equivalent fracture mechanics approach has been used to introduce a characteristic length scale $c_f^{(i)}$. This length is associated with the FPZ size, and it is treated as a material property along with $G_f^{(i)}$. As a result, the scaling equation depends not only on $G_f^{(i)}$ but also on the FPZ size. Leveraging Eq. (4), an excellent agreement with the experimental nominal strength is shown, including the transition from quasi-ductile to brittle behavior as the size increases. The mode I fracture energy is found to be 0.56 N/mm, whereas the mode II fracture energy, defined here as a material property, is 2.25 N/mm. The equivalent FPZ lengths are found to be $c_f^{(I)} = 5.82$ mm and $c_f^{(II)} = 33.51$ mm for modes I and II, respectively.
- (6) The difference between the fracture energies predicted by LEFM and SEL depends on the FPZ size compared with the specimen size, with LEFM underestimating $G_f^{(i)}$ compared with SEL. For the DCB specimens investigated in this work, the difference between LEFM and SEL is 18%, 4%, and 2% for the small, medium, and large sizes, respectively. For the ENF specimens, the LEFM predictions are about 55%, 43%, and 40% lower compared with the SEL for the small, medium, and large sizes, respectively. The difference decreases with increasing specimen sizes and tends to zero for sufficiently large specimens, as the FPZ becomes negligible compared with the specimen size.
- (7) Finite element simulations of the DCB and ENF tests by means of a cohesive zone model featuring a linear traction-separation law support the use of SEL for the estimation of the mode I and II fracture energy. In fact, using the energy estimated by SEL as an input for the cohesive model, the agreement with the experimental load-displacement curves is excellent. This also confirms that the use of LEFM to calculate the fracture energy for cohesive zone models would lead to severe errors, especially in regards to the mode II cohesive law.

- (8) The results of this work highlight the importance of understanding the size effect of the fracturing behavior of laminated composites. The size effect testing on radially-scaled specimens and the analysis via quasi-brittle fracture mechanics provide a simple and effective way to address this important aspect. Further, using size effect to estimate the mode I and II interlaminar fracture properties is easier than other methods because only the peak load measurements are necessary, and no information on the post-peak is required. This is particularly advantageous for interlaminar fracture tests that are often affected by snap-back instability or discontinuous crack propagation, which make visual observations impractical and inaccurate.

Acknowledgment

This material is based upon work supported by the Department of Energy (Funder ID: 10.13039/100000015) under Cooperative Award Number DE-EE0005661 to the United States Automotive Materials Partnership, LLC and sub-award SP0020579 to Northwestern University. The work was also partially supported under NSF (Funder ID: 10.13039/100000001) grant No. CMMI-1435923 to Northwestern University.

References

- [1] Lukaszewicz, D., 2013, "Automotive Composite Structures for Crashworthiness," *Advanced Composite Materials for Automotive Applications: Structural Integrity and Crashworthiness*, A. Elmarakbi, ed., Wiley, New York, pp. 100–127.
- [2] Rana, S., and Fangueiro, R., 2016, *Advanced Composites Materials for Aerospace Engineering*, Woodhead Publishing, Amsterdam.
- [3] Song, D., and Gupta, R., 2012, "The Use of Thermosets in the Building and Construction Industry," *Thermosets: Structure, Properties, and Applications*, Q. Guo, ed., Elsevier, New York, pp. 165–188.
- [4] Stenzenberger, H. D., 1993, "Recent Developments of Thermosetting Polymers for Advanced Composites," *Compos. Struct.*, **24**(3), pp. 219–231.
- [5] Pascault, R., and Williams, J., 2018, "Overview of Thermosets: Present and Future," *Thermosets: Structure, Properties, and Applications*, Q. Guo, ed., Elsevier, New York, pp. 3–34.
- [6] Wan, Y., and Takahashi, J., 2016, "Tensile and Compressive Properties of Chopped Carbon Fiber Tapes Reinforced Thermoplastics With Different Fiber Lengths and Molding Pressures," *Compos. Part A*, **87**, pp. 271–281.
- [7] Blok, L. G., Longana, M. L., Yu, H., and Woods, B. K. S., 2018, "An Investigation Into 3D Printing of Fibre Reinforced Thermoplastic Composites," *Addit. Manuf.*, **22**, pp. 176–186.
- [8] Yao, S. S., Jin, F. L., Rhee, K. Y., Hui, D., and Park, S. J., 2018, "Recent Advances in Carbon-fiber-Reinforced Thermoplastic Composites: A Review," *Compos. Part B*, **142**, pp. 241–250.
- [9] Biron, M., 2018, *Thermoplastics and Thermoplastic Composites, Plastics Design Library*, Elsevier, Amsterdam, pp. 1083–1126.
- [10] Ceccato, C., Salviato, M., Pellegrino, C., and Cusatis, G., 2017, "Simulation of Concrete Failure and Fiber Reinforced Polymer Fracture in Confined Columns With Different Cross Sectional Shape," *Int. J. Solids Struct.*, **108**, pp. 216–229.
- [11] Cox, B. N., Dadkhah, M. S., Morris, W. L., and Flintoff, J. G., 1994, "Failure Mechanisms of 3D Woven Composites in Tension, Compression, and Bending," *Acta Metall. Mater.*, **42**(12), pp. 3967–3984.
- [12] Long, A. C., 2005, *Design and Manufacturing of Textile Composites*, Cambridge University Press, Cambridge.
- [13] Bogdanovich, A. E., 2000, "Three-Dimensional Variational Theory of Laminated Composite Plates and Its Implementation With Bernstein Basis Functions," *Comput. Methods Appl. Mech. Eng.*, **185**(2–4), pp. 279–304.
- [14] Bogdanovich, A. E., 2006, "Multi-Scale Modeling, Stress and Failure Analyses of 3-D Woven Composites," *J. Mater. Sci.*, **41**(20), pp. 6547–6590.
- [15] Pankow, M., Salvi, A., Waas, A. M., Yen, C. F., and Ghiorse, S., 2011, "Resistance to Delamination of 3D Woven Textile Composites Evaluated Using End Notch Flexure (ENF) Tests: Experimental Results," *Compos. Part A*, **42**(10), pp. 1463–1476.
- [16] Mouritz, A. P., Leong, K. H., and Herszberg, I., 1997, "A Review of the Effect of Stitching on the In-Plane Mechanical Properties of Fibre-Reinforced Polymer Composites," *Compos. Part A*, **28**(12), pp. 979–991.
- [17] Maloney, K., and Fleck, N., 2018, "Damage Tolerance of An Architected Adhesive Joint," *Int. J. Solids Struct.*, **132**, pp. 9–19.
- [18] Bažant, Z., and Planas, J., 1998, *Fracture and Size Effect in Concrete and Other Quasi-brittle Materials*, CRC Press, Boca Raton.
- [19] Salviato, M., Kirane, K., Ashari, S., Bažant, Z., and Cusatis, G., 2016, "Experimental and Numerical Investigation of Intra-Laminar Energy Dissipation and Size Effect in Two-Dimensional Textile Composites," *Compos. Sci. Technol.*, **135**, pp. 67–75.
- [20] ASTM D3039, 2014, "Standard Test Method for Tensile Properties of Polymer Matrix Composite Materials".
- [21] ASTM D3518, 2014, "Standard Test Method for In-Plane Shear Response of Polymer Matrix Composite Materials by Tensile Test of a ±45° Laminate".
- [22] Salviato, M., Chau, V. T., Li, W., Bažant, Z. P., and Cusatis, G., 2016, "Direct Testing of Gradual Postpeak Softening of Fracture Specimens of Fiber Composites Stabilized by Enhanced Grip Stiffness and Mass," *J. Appl. Mech.*, **83**(11), p. 111003.
- [23] Salviato, M., Ashari, S. E., and Cusatis, G., 2016, "Spectral Stiffness Microplane Model for Damage and Fracture of Textile Composites," *Compos. Struct.*, **137**, pp. 170–184.
- [24] Kirane, K., Salviato, M., and Bažant, Z. P., 2016, "Microplane-Triad Model for Elastic and Fracturing Behavior of Woven Composites," *J. Appl. Mech.*, **83**(4), p. 041006.
- [25] Kirane, K., Salviato, M., and Bažant, Z. P., 2016, "Microplane Triad Model for Simple and Accurate Prediction of Orthotropic Elastic Constants of Woven Fabric Composites," *J. Compos. Mater.*, **50**(9), pp. 1247–1260.
- [26] ASTM D5528, 2007, "Standard Test Method for Mode I Interlaminar Fracture Toughness of Unidirectional Fiber-Reinforced Polymer Matrix Composites".
- [27] Cantwell, W. J., 1997, "The Influence of Loading Rate on the Mode II Interlaminar Fracture Toughness of Composite Materials," *J. Compos. Mater.*, **31**(14), pp. 1364–1380.
- [28] Sousa, J. A., Pereira, A. B., Martins, A. P., and de Moraes, A. B., 2015, "Mode II Fatigue Delamination of Carbon/epoxy Laminates Using the End-notched Flexure Test," *Compos. Struct.*, **134**, pp. 506–512.
- [29] Carraro, P.A., Meneghetti, G., Quaresimin, M., and Ricotta, M., 2013, "Crack Propagation Analysis in Composite Bonded Joints Under Mixed-mode (I+II) Static and Fatigue Loading: A Damage-based Model," *J. Adhes. Sci. Technol.*, **27**(13), pp. 1393–1406.
- [30] Cusatis, G., and Schaufert, E. A., 2009, "Cohesive Crack Analysis of Size Effect," *Eng. Fract. Mech.*, **76**(14), pp. 2163–2173.
- [31] Quaresimin, M., Salviato, M., and Zappalorto, M., 2012, "Fracture and Interlaminar Properties of Clay-Modified Epoxies and Their Glass Reinforced Laminates," *Eng. Fract. Mech.*, **81**, pp. 80–93.
- [32] Bažant, Z. P., 1984, "Size Effect in Blunt Fracture: Concrete, Rock, Metal," *J. Eng. Mech. ASCE*, **110**(4), pp. 518–535.
- [33] Bažant, Z. P., and Kazemi, M. T., 1990, "Determination of Fracture Energy, Process Zone Length and Brittleness Number From Size Effect, With Application to Rock and Concrete," *Int. J. Fract.*, **44**(2), pp. 111–131.
- [34] Bažant, Z. P., Daniel, I. M., and Li, Z., 1996, "Size Effect and Fracture Characteristics of Composite Laminates," *J. Eng. Mater.-T ASME*, **118**(3), pp. 317–24.
- [35] Mefford, C. H., Qiao, Y., and Salviato, M., 2017, "Failure Behavior and Scaling of Graphene Nanocomposites," *Compos. Struct.*, **176**, pp. 961–972.
- [36] Qiao, Y., and Salviato, M., 2019, "Study of the Fracturing Behavior of Thermoset Polymer Nanocomposites Via Cohesive Zone Modeling," *Compos. Struct.*, **220**, pp. 127–147.
- [37] Hoover, C., and Bažant, Z., 2019, "Strength and Cohesive Behavior of Thermoset Polymers at the Microscale: A Size-Effect Study," *Eng. Fract. Mech.*, **213**, pp. 100–117.
- [38] ABAQUS, 2013, *ABAQUS Users Manual, Version 6.13-1*, Hibbit, Karlson and Sorenson, Pawtucket, RI.
- [39] Barsoum, R. S., 1976, "A Degenerate Solid Element for Linear Fracture Analysis of Plate Bending and General Shells," *Int. J. Numer. Meth. Eng.*, **10**(3), pp. 551–564.
- [40] Rice, J. R., 1968, "A Path Independent Integral and the Approximate Analysis of Strain Concentration by Notches and Cracks," *ASME J. Appl. Mech.*, **35**(2), pp. 379–386.
- [41] Williams, J. G., 1989, "End Corrections for Orthotropic DCB Specimens," *Compos. Sci. Technol.*, **35**(4), pp. 367–376.
- [42] Williams, J. G., and Hadavinia, H., 2002, "Analytical Solutions for Cohesive Zone Models," *J. Mech. Phys. Solids*, **50**(4), pp. 809–825.
- [43] Soykasan, O., Pellegrino, S., Howard, P., and Notter, M., 2008, "Folding Large Antenna Tape Spring," *J. Spacecraft Rockets*, **45**(3), pp. 560–567.
- [44] Mallikarachchi, H. M. Y. C., and Pellegrino, S., 2011, "Quasi-Static Folding and Deployment of Ultrathin Composite Tape-spring Hinges," *J. Spacecraft Rockets*, **48**(1), pp. 187–198.
- [45] Hoover, C. G., and Bažant, Z. P., 2014, "Cohesive Crack, Size Effect, Crack Band and Work-of-fracture Models Compared to Comprehensive Concrete Fracture Tests," *Int. J. Fract.*, **187**(1), pp. 133–143.